Energy and force prediction for a nanosecond pulsed dielectric barrier discharge actuator

Chin-Cheng Wang and Subrata Roy

Citation: J. Appl. Phys. **111**, 103302 (2012); doi: 10.1063/1.4722202
View online: http://dx.doi.org/10.1063/1.4722202
View Table of Contents: http://jap.aip.org/resource/1/JAPIAU/v111/i10
Published by the American Institute of Physics.

Energy and force prediction for a nanosecond pulsed dielectric barrier discharge actuator

Chin-Cheng Wang[a] and Subrata Roy[b]
Applied Physics Research Group, Department of Mechanical and Aerospace Engineering, University of Florida, Gainesville, Florida 32611, USA

(Received 12 February 2012; accepted 28 April 2012; published online 30 May 2012)

A three-species physical model is presented for dielectric barrier discharge (DBD) actuator under atmospheric pressure. The governing equations are solved for temporal and spatial distribution of electric potential and charge species using the finite element based multiscale ionized gas flow code. The plasma model is loosely coupled with compressible Navier-Stokes equations through momentum and energy source terms. Two cases of rf powered and nanosecond pulsed barrier discharge actuators are simulated. Based on the imparted time average electrohydrodynamic force and power deposition to the neutral gas, the nanosecond pulsed DBD actuator creates significant pressure variations within few microseconds. These results are in reasonable agreement with recently reported experimental shadow images. © *2012 American Institute of Physics*.
[http://dx.doi.org/10.1063/1.4722202]

I. INTRODUCTION

Weakly ionized plasmas in dielectric barrier discharge (DBD) generated using moderate frequency high voltage power source have been applied to a number of applications in the past few decades.[1] At the present time, applications such as sterilization[2] for healthcare purposes, flow control[3] for the aerospace industries, and flame stability[4] for the combustion engines are potentially very exciting areas. However, non-equilibrium DBD plasmas find limited application for high speed flows. This is due to inherent losses associated with the momentum exchange between the charged and neutral particles and due to exorbitant power budget. As an alternative, high-voltage nanosecond pulsed DBD plasmas[5] are becoming quite attractive option for high speed application.

In conventional method, non-equilibrium plasmas can be generated between two electrodes on the dielectric surface as an alternating current (AC) passes through them with high sinusoidal voltage. The dielectric is used to stabilize the discharge without arcing. Such a plasma generating device is called a DBD actuator. The operational conditions of the DBD actuator are at frequencies of one to tens of kilohertz and amplitudes of one to tens of kilovolts in a sinusoidal type wave. Our recent experiments[6] showed such conventional AC powered DBD actuator consumes tens of watts per meter under atmospheric pressure. The value of the power increased exponentially as the input applied voltage increased linearly from 14 to 30 kV. If we can minimize the power required to sustain non-equilibrium plasmas, such plasma generating device will become very useful.

There are a few ways to sustain non-equilibrium plasmas with low input applied voltage such as microscale discharges[7–9] and nanosecond pulsed discharges.[10–12] Macheret *et al.*[5] presented analytical calculations showing that power budget in nanosecond pulsed discharges can be significantly lower than that in dc discharges. They predicted an ionization efficiency (i.e., ionization level/power) improvement of roughly two orders of magnitude. Also, their modeling showed there is a strong ionization near the cathode sheath due to non-uniform redistribution of electric potential. Later on, the Princeton University group showed both numerical and experimental investigations of the DBD actuators driven by nanosecond pulses.[10,11] Both computations and experiments demonstrated the similar vortical structures induced by the actuator. Also, the results showed repetitive short pulses do efficiently generate the plasma.

Recently, experimental results of nanosecond pulsed plasma actuator by Starikovskii *et al.*[12] have reported that nanosecond pulsed voltage is highly efficient to control boundary layer separation, lift and drag force coefficients, in addition to acoustic noise reduction in the Mach number range 0.05–0.85 compared with AC sinusoidal voltage. More significantly, they concluded that there is a fundamental difference between nanosecond pulsed discharge and conventional AC driven discharge for the plasma-flow interaction. In the case of conventional DBD actuator, the main mechanism of impact is the momentum transfer from electric field to the near surface gas. In contrast, for nanosecond pulsed DBD actuator, the main mechanism of impact is the energy transfer to the gas near the surface. Their measurements showed the mean values of such heating can reach 400 K for 50 ns pulse durations. Such fast heating (less than microsecond) of the gas layer leads to periodic flow disturbances that control boundary layer separation and reduce acoustic noise at the Mach number close to one.

Subsequently, Unfer and Boeuf[13] presented a self-consistent model for nanosecond pulsed actuator. They showed spatial and temporal distribution of the gas pressure perturbation induced by the discharge. These results have been qualitatively compared with Starikovskii *et al.*[12] However, a detailed study of the physics of nanosecond pulsed

[a]Present address: Department of Mechanical Engineering, Yuan Ze University, Chung-Li, Taoyuan 32003, Taiwan.
[b]E-mail: roy@ufl.edu.

DBD actuator is crucial for improving the design and performance of such device.

The aim of this work is to simulate and compare the differences between conventional AC DBD and nanosecond pulsed DC DBD to understand the physics of plasma-flow interactions induced by above two different modes. In the experiment of phase-locked particle image velocimetry,[14] authors found the negative ions play a dominant role in plasma actuation. Therefore, it is important to implement a three-species plasma model including positive ions, negative ions, and electrons. Simulation details of these charged species using a drift-diffusion form fully coupled with Possion's equation for electric potential are given in Sec. II. This physical model has been widely used and gives reasonable electro-hydrodynamic (EHD) force distribution to the neutral gas. Section III describes numerical approach of finite element based multiscale ionized gas (MIG) flow code. Section IV presents the computational domain and simulation results for two specific cases simulated, namely, radio frequency (RF) powered and nanosecond pulsed DBD actuators. Conclusions are summarized in Sec. V.

II. NUMERICAL MODELING

A three-species hydrodynamic model[10,13] is employed for multi-scale plasma discharge simulation at atmospheric pressure. The model uses an efficient finite element algorithm. The unsteady transport for positive ions, negative ions, as well as electrons is derived from fluid dynamics in the form of mass and momentum conservation equations. The species momentum is modeled using the drift-diffusion approximation under isothermal condition that can be derived from the hydrodynamic equation. At atmospheric pressure, the drift-diffusion approximation is reasonable and computationally efficient. The continuity equations for positive ions, negative ions, and electrons are given by

$$\frac{\partial n_p}{\partial t}+\frac{\partial (n_p V_j)}{\partial x_j}=\alpha|\Gamma_e|-r_{ep}n_p n_e-r_{mp}n_p n_m, \tag{1}$$

$$\frac{\partial n_m}{\partial t}+\frac{\partial (n_m V_j)}{\partial x_j}=\eta|\Gamma_e|-r_{mp}n_m n_p, \tag{2}$$

$$\frac{\partial n_e}{\partial t}+\frac{\partial (n_e V_j)}{\partial x_j}=(\alpha-\eta)|\Gamma_e|-r_{ep}n_e n_{pe}, \tag{3}$$

$$|\Gamma_e|=\sqrt{\sum_j (n_e V_j)^2}, 1\le j\le 2, \tag{4}$$

where $n_{p,m,e}$ are the number densities of the charged particle, subscript p, m, and e are positive ions, negative ions, and electrons, respectively. $V_{p,m,e}$ are the species hydrodynamic velocities, α is the ionization coefficient, η is the attachment coefficient, $r_{ep,mp}$ are the electron-ion and ion-ion recombination coefficients, $|\Gamma_e|$ is the electronic flux, and subscript j is the coordinate direction (i.e., $j=x, y$). Here, we neglect the magnetic field effect in the drift-diffusion approximation. The ionic and electronic fluxes in Eqs. (1)–(3) are written as

$$n_p V_p=n_p\mu_p\mathbf{E}-D_p\nabla n_p, \tag{5}$$

$$n_m V_m=-n_m\mu_m\mathbf{E}-D_m\nabla n_m, \tag{6}$$

$$n_e V_e=-n_e\mu_e\mathbf{E}-D_e\nabla n_e, \tag{7}$$

where the electrostatic field is given by $\mathbf{E}=-\nabla\phi$, $\mu_{p,m,e}$ are the charged particle mobilities, which are based on tabulated functions of the reduced electric field (E/N),[15] $D_{p,m,e}$ are the diffusion coefficients calculated from the Einstein relation $D_{p,m,e}=\mu_{p,m,e}\,k_B\,T_{p,m,e}/e$, which is a function of the mobility ($\mu_{p,m,e}$), Boltzmann's constant (k_B), the constant temperatures ($T_{p,m}=300\,\mathrm{K}$ and $T_e=11600\,\mathrm{K}$), and the elementary charge ($e=1.6022\times10^{-19}$ C). The ion and electron drift velocities depend mainly on the electric field. So all the transport coefficients are expressed as a function of a reduced electric field (E/N). The working gas is an air-like N_2/O_2 mixture. The mobilities, diffusion rates, and rate coefficients for air-like mixture are obtained from the Refs. 15–17. The relation between electric field ($\mathbf{E}$) and charge separation (q) is given by the Poisson's equation

$$\nabla\cdot(\varepsilon\mathbf{E})=e(n_p-n_m-n_e)=q, \tag{8}$$

where ε is the permittivity.

The coupled systems of species Eqs. (1)–(3) as well as Poisson's Eq. (8) are solved using the in-house MIG flow code described in Sec. III. The following boundary conditions are enforced. At the exposed electrode, the electronic flux is based on the electron thermal velocity and is directed towards the electrode. The positive ion flux normal to the exposed electrode is considered as zero if the electric field is greater than zero. In the plasma domain of top, left, and right boundaries, the homogeneous Neumann boundary condition is imposed (i.e., the slopes of the solution variables are equal to zero). The initial ion and electron number densities are assumed to be uniform and equal to 10^{15} m^{-3} in the plasma domain, while the charged particle densities are equal to zero in the dielectric material.

The effect of plasma actuation and the gas heating are incorporated into the compressible Navier-Stokes flow equations through the time-averaged source terms shown below

$$\frac{\partial\rho}{\partial t}+\nabla\cdot(\rho\mathbf{V_n})=0, \tag{9}$$

$$\frac{\partial(\rho\mathbf{V_n})}{\partial t}+\nabla\cdot(\rho\mathbf{V_n}\mathbf{V_n})=-\nabla p+\nabla\cdot(\boldsymbol{\tau})+\mathbf{F_E}, \tag{10}$$

$$\frac{\partial(\rho E_n)}{\partial t}+\nabla\cdot[\mathbf{V_n}(\rho E_n+p)]=\nabla\cdot(k\nabla T_n+\boldsymbol{\tau}\cdot\mathbf{V_n})+\mathbf{P_{Th}}, \tag{11}$$

where ρ is the fluid density, $\mathbf{V_n}$ is the neutral gas velocity, p is the pressure, $\boldsymbol{\tau}$ is the stress tensor, E_n is the total specific energy, k is the conductivity, and T_n is the neutral gas temperature. For the momentum equations, the electric force density is described as $\mathbf{F_E}=\frac{1}{w}\left[\sum_{i=1}^{w} e(n_p-n_m-n_e)\mathbf{E}\right]$, and w is the number of time stations in a cycle used for time-averaging. For the energy equations, the power deposition can be assumed as $\mathbf{P_{Th}}=\frac{1}{w}\left[\sum_{i}^{w}(\mathbf{J}_p-\mathbf{J}_m)\cdot\mathbf{E}-\xi_{EX}\mathbf{J}_e\cdot\mathbf{E}\right]$, where $\mathbf{J}$ is the current density and ξ_{EX} is the 28% of the

electron energy deposited into excited states of the gas.[18] A commercial flow solver, ANSYS FLUENT, is used for flow simulation where EHD force $\mathbf{F_E}$ and gas heating $\mathbf{P_{Th}}$ are incorporated as source terms in the momentum and energy equations via user defined functions (UDFs).

III. NUMERICAL APPROACH

The plasma modeling approach uses an efficient, parallel, finite element algorithm[19] anchored in the MIG flow code. MIG is a modular code and has been developed and verified with one-, two-, and three-dimensional plasma and fluid-thermal problems. These problems include slip/transitional flows through micro/nanoscale geometries, modeling of the Hall effect thrusters using multispecies and two-temperature physics. Specifically, MIG has been used to model dielectric barrier discharges for subsonic flow control at atmospheric conditions.[3,4,7–9] The finite element based modeling allows boundary conditions to be easily implemented.

Systems of nonlinear partial differential equations can be solved using the finite element based MIG code. If we denote the differential equation using an operator $L(\cdot)$, then the system of equations can be written as $L(\theta) = 0$ where θ is the unknown state variables. Multiplying this equation by a permissible test function ψ and integrating over a discretized domain Ω yields the Galerkin weak statement (GWS). The test function in the GWS is chosen orthogonal to the trial function to ensure the minimum error. The resulting matrix equation is solved with the nonlinear Newton-Raphson scheme using a generalized minimal residual (GMRES) solver to handle the sparseness of the stiffness matrix. The system utilizes a subgrid embedded (SGM) algorithm[20] for computational stability and control of dispersion error. The SGM algorithm is incorporated into the dissipative flux terms based on the local cell velocity and is expected to ensure a nodewise monotone solution. For plasma application in 2-D, a nodally distribution (subscript i) SGM parameter is $r_i = \frac{|V_i|h_i}{\gamma_i D_i}$, where the $\gamma_i = \sqrt{\frac{1 \cdot A_e}{D_i h_i}}$ is a correlation function, V_i is the drift velocity, h_i is the element size, D_i is the diffusion parameter, and A_e is the area of the element. The convergence criterion is based on the L_2 norms of the change in the solution $\Delta\theta$ and the residual at each time step. The convergence criterion for the problem is met when the residuals for all state variables fall below a chosen number of 10^{-4}.

In the present work, we assume that the plasma effects can be loosely coupled to the compressible Navier-Stokes equations through the body force and energy source terms, which depend on the net space charge, ionic, and electronic fluxes as well as electric field distributions. Due to large time scales difference between electrons (nanosecond), ions (i.e., microsecond), and fluid flow (i.e., millisecond), we neglect the flow effect on the plasma formation.

IV. RESULTS AND DISCUSSION

A. Computational domain

Figures 1(a) and 1(b) show the computational dimensions of 1×0.5 cm^2 for the plasma domain and 3×1 cm^2 for the fluid flow domain, respectively. These grids correspond the sizes of 90 321 and 60 701 nodes, respectively. The smallest cell size is 25 μm for both domains suitable to resolve the sheath structure. Figure 1(c) shows a zoomed in view of the DBD actuator. The DBD actuator consists of two electrodes separated by a 0.1 mm thick dielectric layer of relative constant $\varepsilon = 5\varepsilon_0$ (where $\varepsilon_0 = 8.854 \times 10^{-12}$ F/m is the permittivity in vacuum). Both exposed power and buried ground electrodes are 2 mm long. The thickness of the electrodes is assumed to be negligible. Also, the gap between electrodes in horizontal direction is assumed to be zero.

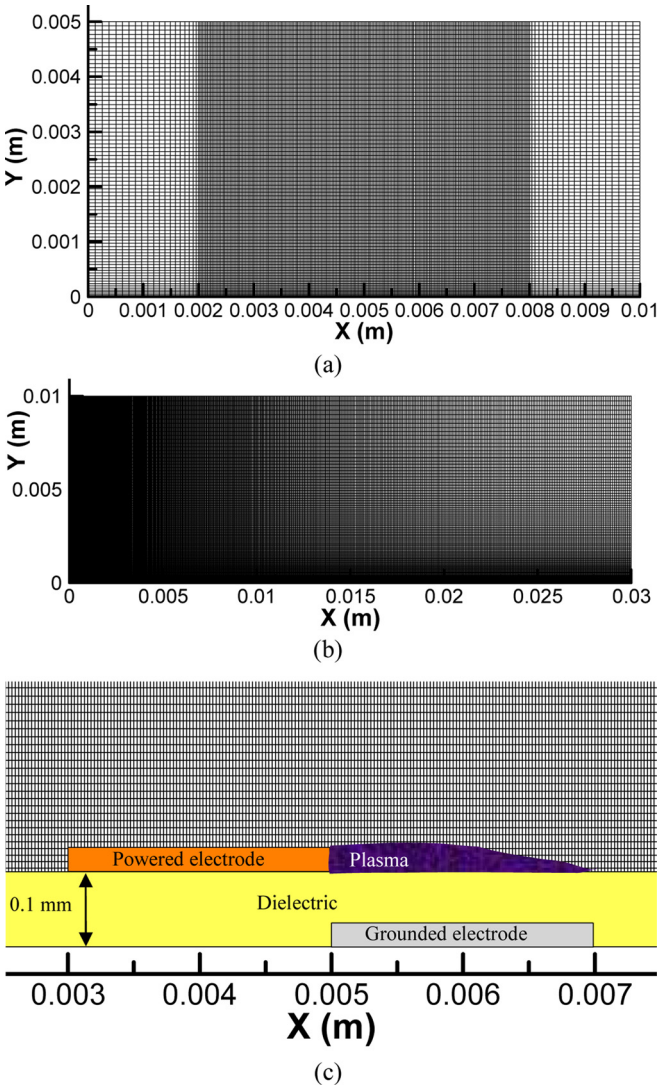

FIG. 1. The computational grids of (a) plasma domain and (b) fluid flow domain. (c) Zoom of the dielectric barrier discharge actuator near the plasma region.

In order to understand the physics of plasma force mechanism for flow control, we present two cases of RF powered and nanosecond pulsed DBD actuators. Figure 2 shows the calculated total linear current density and applied voltage for these two different modes. For the case of RF powered DBD actuator, the exposed electrode is driven by sinusoidal waveform with amplitude of 0.5 kV and frequency of 1000 kHz. We can consider a period of time from 4.5 μs to 5.5 μs for the sine wave shown in Figure 2. There are two slopes, which are the positive-going (when the slope of the applied

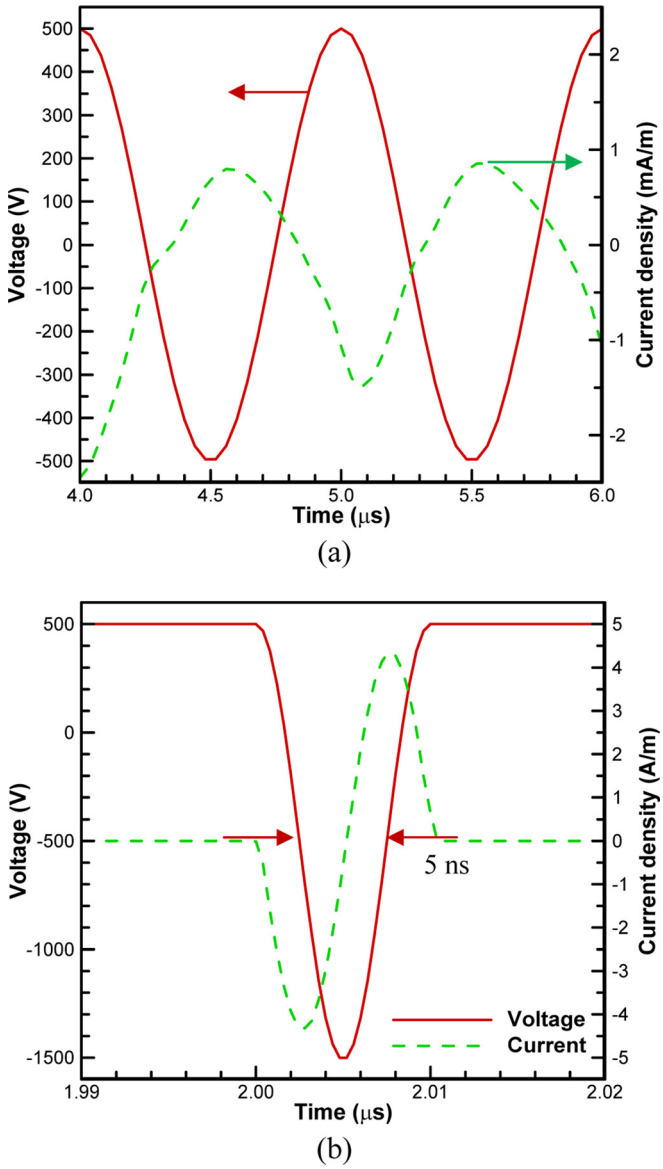

FIG. 2. Calculated total linear current density (dashed line) and applied voltage (solid line) for (a) amplitude of 0.5 kV and frequency of 1000 kHz sinusoidal waveform and (b) nanosecond pulse of −2 kV amplitude with repetition rate of 500 kHz superimposed on a dc bias of 0.5 kV; FWHM of 5 ns.

voltage is positive) and the negative-going (opposite direction of the positive-going) discharges. We can see an uneven peak linear current density passing through the exposed electrode for both slopes. The peak linear current density estimates around 1 mA/m for the positive-going discharge and 1.5 mA/m for the negative-going discharge. The uneven peak linear current density may explain why the forward EHD force (i.e., momentum transfer) dominates the flow field. For the case of nanosecond pulsed DBD actuator, the exposed electrode is driven by negative pulses of −2 kV amplitude and repetition rates of 500 kHz superimposed on a positive dc bias shown in Figure 2(b). The full width at half maximum (FWHM) of the pulse is 5 ns. The calculated total linear current density of the nanosecond pulsed actuator is much higher than the RF powered actuator. This instantaneous surge may be the reason why the gas heating (i.e., energy transfer) becomes the main mechanism of impact for the nanosecond pulsed DBD actuator.

B. Plasma dynamics for RF powered DBD actuator

In order to understand the physics of RF powered DBD actuator, we can consider two separate slopes of sine wave. Figure 3 shows the electric potential, net charges, force, and power density distribution at 4.56 μs (i.e., positive-going discharge). At this instant, the electric potential varies from −465 to 0 V shown in Figure 3(a). During the negative half-cycle of the discharge, the exposed electrode (colored by orange) plays the role of the cathode (i.e., emits electrons if electric field is high enough). Some electrons may escape from molecules or atoms due to ionization process. Some electrons may attach to oxygen and form negative ions. The net charge separation is based on the temporal and spatial distribution of these positive ions, negative ions, and electrons shown in Figure 3(b). Figure 3(c) shows the horizontal force magnitude overlaid on force vectors. While the positive ions are attracted to the cathode (i.e., exposed electrode), the part of the horizontal force vectors is acting to the left based on the direction of the electric field. At this instant, the peak of the power deposition is around six orders of magnitude shown in Figure 3(d). For the negative-going discharge shown in Figure 4, we can see the same style of contours for electric potential, net charge separation, horizontal force magnitude overlaid on force vectors, and power deposition at 5.08 μs. The peak applied voltage is equal to 438 V at the exposed electrode shown in Figure 4(a). During this positive half-cycle of the discharge, the negative ions and electrons are attracted by the anode (i.e., the exposed electrode), while the positive ions move towards the dielectric surface. The strongest net charge is close to the tip of exposed electrode due to very high electric field ($\sim 3 \times 10^6$ V/m). Compared with Figure 3(c), the horizontal force magnitude in Figure 4(c) is much stronger and imparts momentum forward downstream to the neutral gas. For the power deposition, both cycles have very similar energy distribution near the tip of the exposed electrode.

C. Plasma dynamics for nanosecond pulsed DBD actuator

Literature[10,11] shows the combination of dc bias and repetitive nanosecond pulses may efficiently generate the plasma. The reason may be most of discharges happen in the negative-going of a sinusoidal signal.[21] In such powering scheme, the nanosecond pulsed signals generate multiple negative-going discharges and produce stronger effect on the flow than a conventional sine wave. Figures 5 and 6 show the contours of applied voltage, net charge separation, horizontal force overlaid on force vectors, and power deposition at the peak pulse voltage (i.e., potential equals −1.5 kV) and after the pulse (i.e., potential equals 0.5 kV), respectively. Figure 5(a) shows the electric potential varies from −1.5 kV to 0 V corresponding to the signal at 2.0048 μs. We can see high concentration of positive ions and negative ions happen near the tip of the exposed electrode due to strong electric field shown in Figure 5(b). During the negative pulse, we can

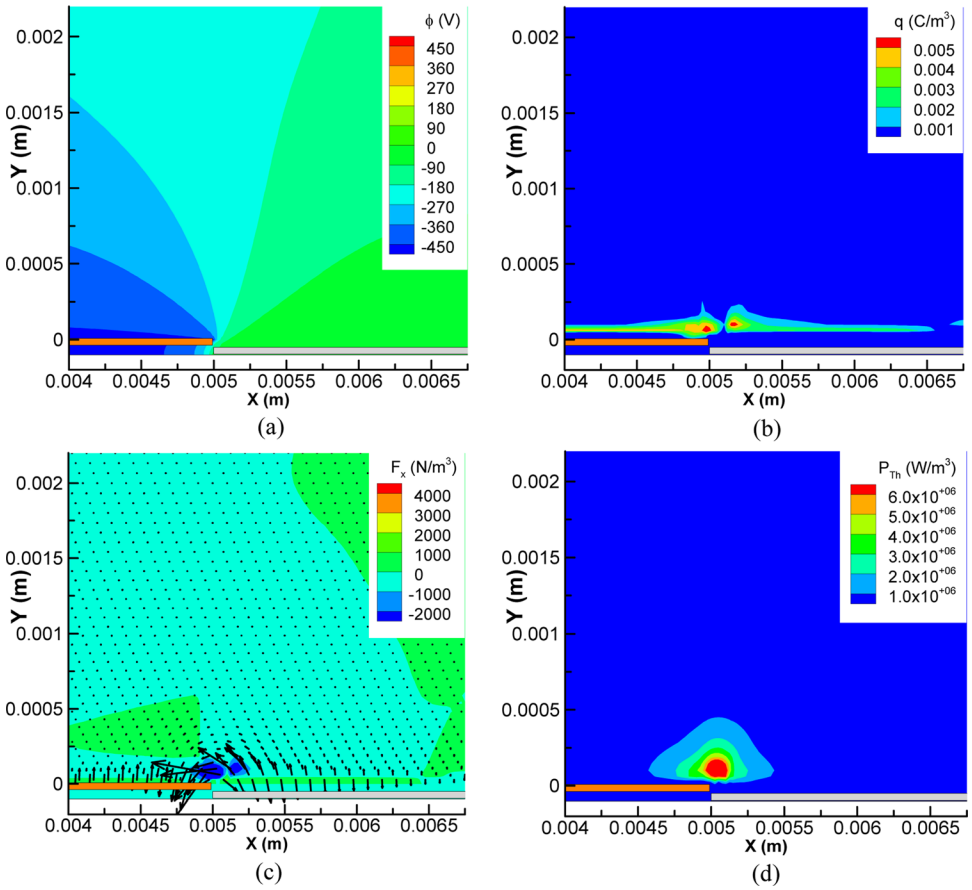

FIG. 3. Contours of (a) electric potential (V), (b) charged separation (C/m^3), (c) horizontal force magnitude (N/m^3) with force vectors, and (d) power deposition (W/m^3) for DBD actuator driven by sinusoidal waveform at 4.56 μs.

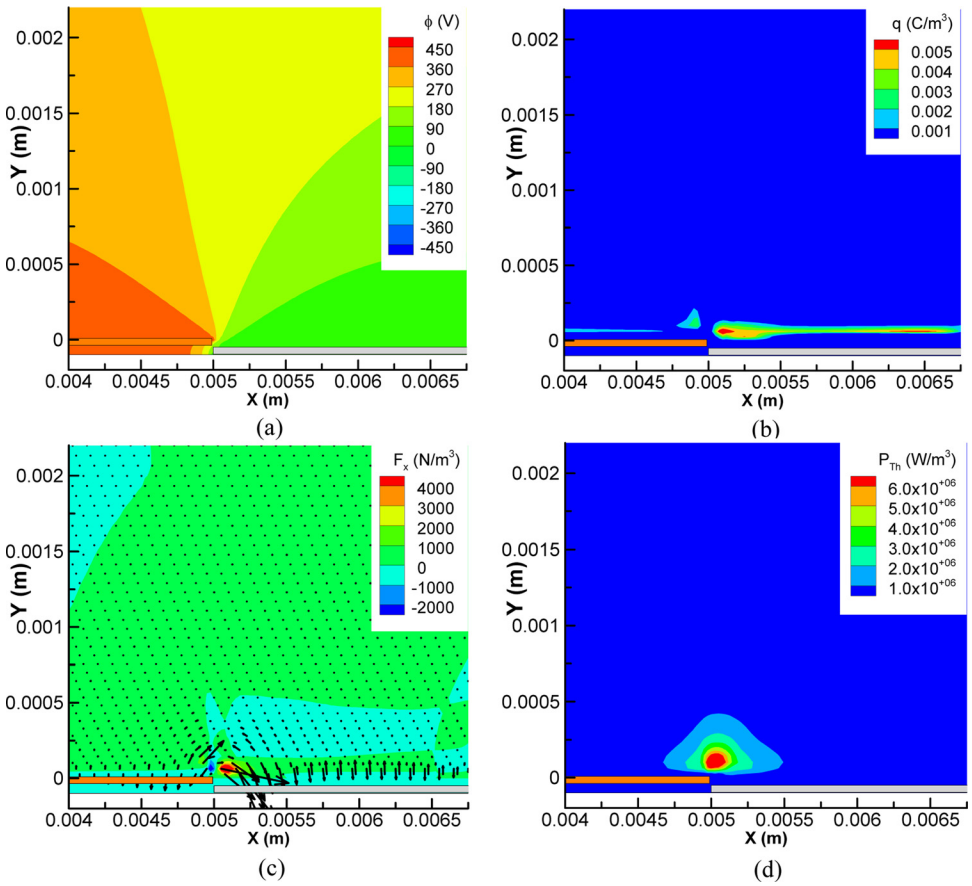

FIG. 4. Contours of (a) electric potential (V), (b) charged separation (C/m^3), (c) horizontal force magnitude (N/m^3) with force vectors, and (d) power deposition (W/m^3) for DBD actuator driven by sinusoidal waveform at 5.08 μs.

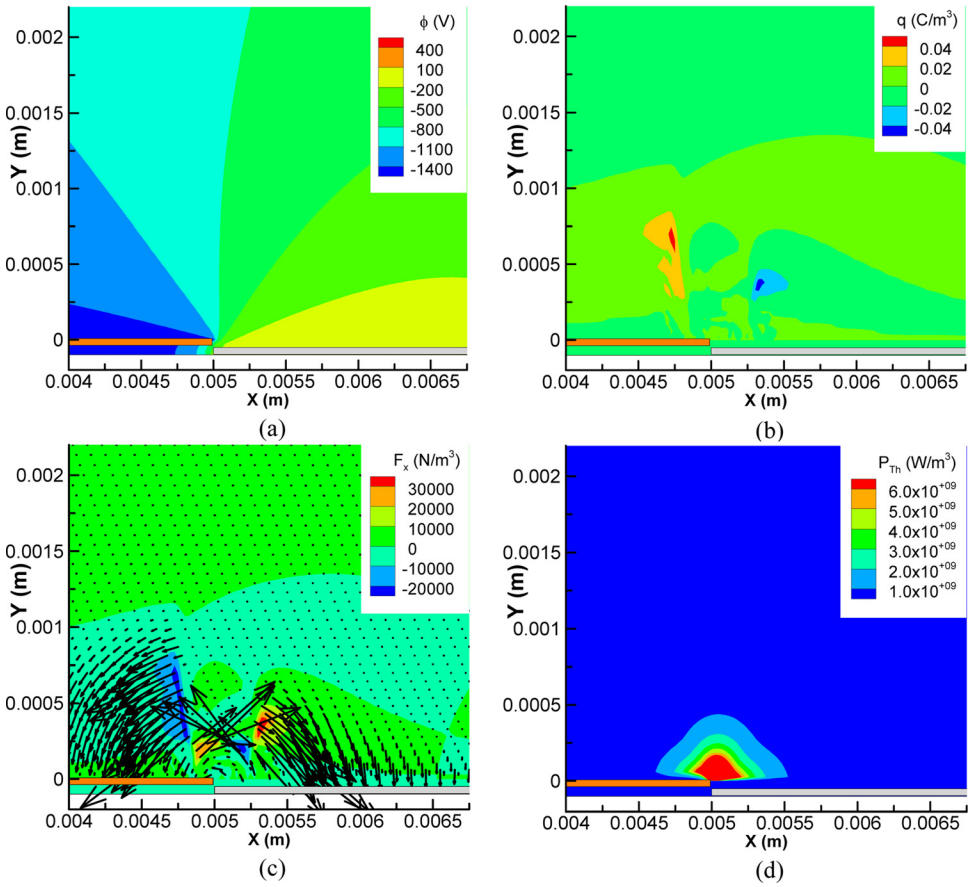

FIG. 5. Contours of (a) electric potential (V), (b) charged separation (C/m^3), (c) horizontal force magnitude (N/m^3) with force vectors, and (d) power deposition (W/m^3) for nanosecond pulsed DBD actuator driven at 2.0048 μs.

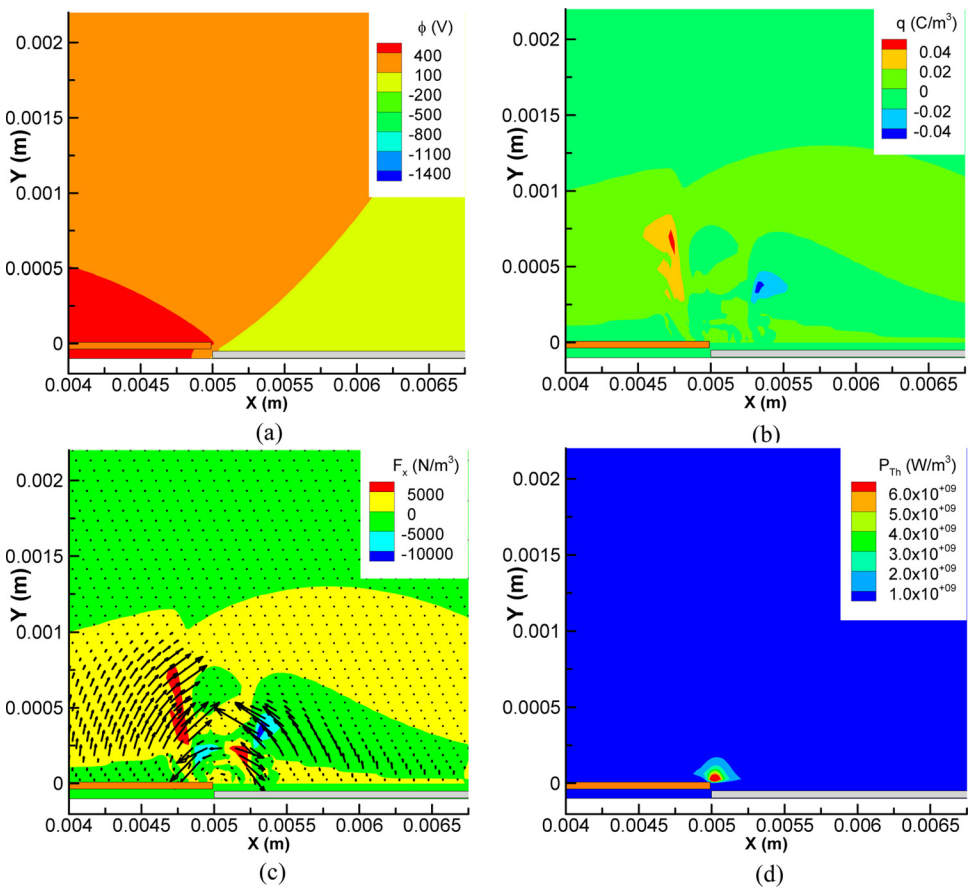

FIG. 6. Contours of (a) electric potential (V), (b) charged separation (C/m^3), (c) horizontal force magnitude (N/m^3) with force vectors, and (d) power deposition (W/m^3) for nanosecond pulsed DBD actuator driven at 2.01 μs.

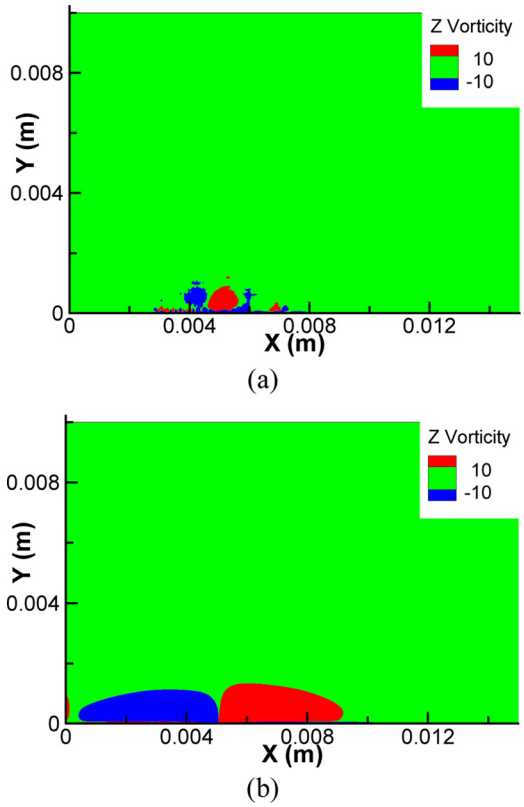

FIG. 7. Contours of z-vorticity induced by (a) RF powered DBD actuator at 10 ms and (b) nanosecond pulsed DBD actuator at 10 μs.

clearly see both upstream-directed force and downstream-directed force on the same orders of magnitude shown in Figure 5(c). After time integration of the negative pulse, the time average of horizontal force becomes small (i.e., tens of N/m^3). Such small amount EHD force may not have significant contribution to momentum transfer. The peak deposited power in W/m^3, shown in Figures 6(d), is of the order of ten that is four orders of magnitude higher than conventional DBD actuator. This may be a reason why the main mechanism of impact is dominated by energy transfer for the nanosecond pulsed DBD actuator.

D. Gas dynamics induced by RF powered and nanosecond pulsed DBD actuator

To see the effects of DBD actuator driven by two different modes, we employ time-averaged EHD force density and power deposition on a quiescent flow domain. Figure 7(a) shows unsteady airflow induced z-vortices by RF powered DBD actuator, while Figure 7(b) plots the airflow generated z-vortices by nanosecond pulsed DBD actuator. For both cases, the induced velocity is quite small (~0.1–0.2 m/s) at this low-voltage of sinusoidal signal and nanosecond pulses. The local body force generated by the RF signal entrains fluid from the upstream to the downstream of the actuator. The vorticity contour near the wall (y = 5 mm) distinct clockwise and counter-clockwise vortex pair due to entrainment and plasma induced jet. The flow response is in milliseconds. For the case of nanosecond pulsed actuator shown in Figure 7(b), the flow response seems quite different. The flow response is very fast within a few microseconds because the flow physics is mainly dominated by energy transfer. The vortices induced by nanosecond pulsed actuator propagate much faster than RF powered actuator. The maximum induced streamwise velocity generated by nanosecond pulses equals 0.23 m/s. This value is on the same order of magnitude with the experimental data from Starikovskii[12] demonstrating that nanosecond pulsed DBD actuator does not induce significant flow velocity.

Figures 8(a)–8(c) show the dynamics of the computed shock wave structure emanating from the nanosecond pulsed

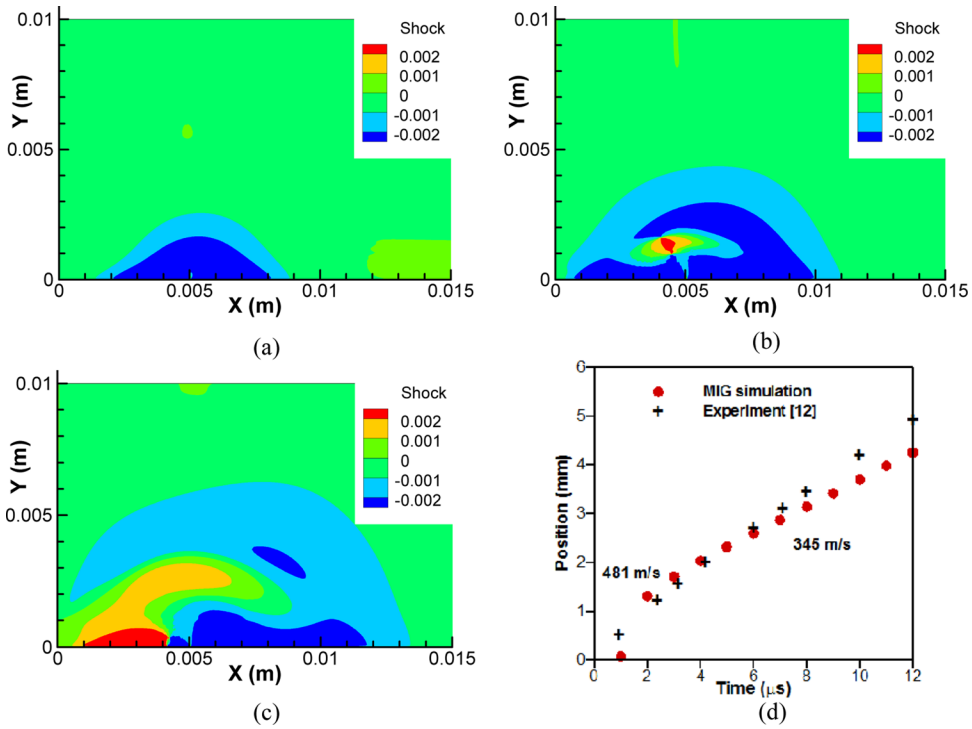

FIG. 8. Contours of shock wave induced by nanosecond pulsed DBD actuator at (a) 8 μs, (b) 16 μs, and (c) 25 μs. (d) Calculated pressure wave propagation speed from the surface at location of $x = 5.1$ mm and pressure of 12 Pa compared with experimental data from Starikovskii.[12]

DBD actuator at 8, 16, and 25 μs. The shock is defined as function of $\mathbf{V_n} \cdot \nabla p/(a|\nabla p|)$, where a is the speed of sound. These results show that the semicircular domain within which the pressure variation is increasing with time due to large energy deposition at the tip of the exposed electrode. These results qualitatively compare well with experimental shadow images from Starikovskii *et al.*[12] Also, the propagation velocity of the pressure (p) wave is calculated and plotted in Figure 8(d). During the first two microseconds, we can see the propagation speed is much faster ($\sim$480 m/s) and then quickly decreased to about 280 m/s. The same phenomenon is also observed from experimental data[12] although in that case a sonic speed was estimated for the first twelve microseconds.

V. CONCLUSIONS

We have studied a self-consistent plasma model for RF powered and nanosecond pulsed DBD actuators in air. Three species of positive ions, negative ions, and electrons have taken into account. In order to obtain temporal and spatial distribution of charged species, the coupled system of continuity equations and Poisson's equation are solved based on finite element based MIG flow code. Fluid flow domain is also solved in a loosely coupled manner using time averaged EHD force and power deposition source terms in compressible Navier-Stokes equations. At the beginning of the negative-going part of the cycle at 4.56 μs, the motion of negative ions and electrons generate an EHD force directed toward the grounded electrode. Such time averaged EHD force creates a near wall jet through momentum transfer to the neutral gas. For the case of nanosecond pulsed DBD actuator, the time averaged EHD force is quite small while the scalar thermal energy deposition near the tip of the exposed electrode is large. The gas dynamics induced by energy deposition shows nanosecond pulsed actuator is able to create acoustic pressure waves within a few microseconds. Such acoustic jets may affect the onset of boundary layer separation.

In summary, we compared the charge distribution between sinusoidal DBD and nanosecond pulsed DBD that showed a fundamentally different mechanism in momentum transfer. We also compared the power deposition mechanism between sinusoidal DBD, and nanosecond pulsed DBD that showed a fundamentally different mechanism in energy transfer. Based on these results, we then calculated the average force and power and apply them to find induced vorticity distribution for both cases. The results show that the flow response for nanosecond DBD is much faster and is in microseconds. To our knowledge, this has not been reported elsewhere. We validated our numerical results for nanosecond pulsed DBD with available experimental data and found a good agreement. Important applications are foreseeable for fixed and moving airfoils in airplanes, helicopters, and wind turbines.

[1] T. C. Corke and C. L. Enloe, "Dielectric barrier discharge plasma actuators for flow control," Rev. Fluid Mech. **42**, 505 (2010).
[2] N. Mastanaiah, C.-C. Wang, J. Johnson, and S. Roy, "A computational diagnostic tool for understanding plasma sterilization," in *49th AIAA Aerospace Sciences Meeting and Exhibit*, AIAA Paper 2011-908, 2011.
[3] C.-C. Wang, R. J. Durscher, and S. Roy, "Three-dimensional effects of curved plasma actuators in quiescent air," J. Appl. Phys. **109**, 083305 (2011).
[4] C.-C. Wang and S. Roy, "Combustion stabilization using serpentine plasma actuators," Appl. Phys. Lett. **99**, 041502 (2011).
[5] S. O. Macheret, M. N. Shneider, and R. B. Miles, "Modeling of air plasma generation by repetitive high-voltage nanosecond pulses," IEEE Trans. Plasma Sci. **30**, 1301 (2002).
[6] R. J. Durscher and S. Roy, "Force measurement techniques and preliminary results using aerogels and ferroelectrics for dielectric barrier discharge actuators," in *41st AIAA Fluid Dynamics Conference and Exhibit*, AIAA Paper 2011-3735, 2011.
[7] C.-C. Wang and S. Roy, "Flow shaping using three-dimensional microscale gas discharge," Appl. Phys. Lett. **95**, 081501 (2009).
[8] C.-C. Wang and S. Roy, "Three-dimensional simulation of a micro plasma pump actuator," J. Phys. D: Appl. Phys. **42**, 185206 (2009).
[9] C.-C. Wang and S. Roy, "Microscale plasma actuators for improved thrust density," J. Appl. Phys. **106**, 013310 (2009).
[10] A. V. Likhanskii, M. N. Shneider, S. O. Macheret, and R. B. Miles, "Modeling of dielectric barrier discharge plasma actuator in air," J. Appl. Phys. **103**, 053305 (2008).
[11] D. F. Opaits, A. V. Likhanskii, G. Neretti, S. Zaidi, M. N. Shneider, S. O. Macheret, and R. B. Miles, "Experimental investigation of dielectric barrier discharge plasma actuators driven by repetitive high-voltage nanosecond pulses with dc or low frequency sinusoidal bias," J. Appl. Phys. **104**, 043304 (2008).
[12] A. Y. Starikovskii, A. A. Nikipelov, M. M. Nudnova, and D. V. Roupassov, "SDBD plasma actuator with nanosecond pulse-periodic discharge," Plasma Sources Sci. Technol. **18**, 034015 (2009).
[13] T. Unfer and J. P. Boeuf, "Modeling of a nanosecond surface discharge actuator," J. Phys. D: Appl. Phys. **42**, 194017 (2009).
[14] W. Kim, H. Do, M. G. Mungal, and M. A. Cappelli, "On the role of oxygen in dielectric barrier discharge actuation of aerodynamic flows," Appl. Phys. Lett. **91**, 181501 (2007).
[15] G. J. M. Hagelaar and L. C. Pitchford, "Solving the Boltzmann equation to obtain electron transport coefficients and rate coefficients for fluid models," Plasma Sources Sci. Technol. **14**, 722–733 (2005).
[16] H. W. Ellis, R. Y. Pai, E. W. McDaniel, E. A. Mason, and L. A. Viehland, "Transport properties of gaseous ions over a wide energy range," At. Data Nucl. Data Tables **17**, 177–210 (1976).
[17] I. A. Kossyi, A. Y. Kostinsky, A. A. Matveyev, and V. P. Silakov, "Kinetic scheme of the non-equilibrium discharge in nitrogen-oxygen mixtures," Plasma Sources Sci. Technol. **1**, 207–220 (1992).
[18] A. Flitti and S. Pancheshnyi, "Gas heating in fast pulsed discharges in N_2O_2 mixtures," Eur. Phys. J. Appl. Phys. **45**, 21001 (2009).
[19] A. J. Baker and D. W. Pepper, *Finite Element 1-2-3* (McGraw Hill, 1991).
[20] S. Roy and A. J. Baker, "Nonlinear, subgrid embedded finite-element basis for accurate, monotone, steady CFD solutions," Numer. Heat Transfer, Part B **31**, 135–176 (1997).
[21] C. L. Enloe, M. G. McHarg, and T. E. McLaughlin, "Time-correlated force production measurements of the dielectric barrier discharge plasma aerodynamic actuator," J. Appl. Phys. **103**, 073302 (2008).